EVOLUTION OF INVISIBLE Au IN ARSENIAN PYRITE IN CARLIN-TYPE Au DEPOSITS

Qing-Lin Liang,[1,2,°] Zhuojun Xie,[1,°] Xie-Yan Song,[1,†] Richard Wirth,[3] Yong Xia,[1] and Jean Cline[4]

[1]*State Key Laboratory of Ore Deposit Geochemistry, Institute of Geochemistry, Chinese Academy of Sciences, Guiyang 550081, China*

[2]*University of Chinese Academy of Sciences, Beijing 100039, China*

[3]*German Research Centre for Geosciences GFZ, 3.5 Surface Geochemistry, Telegrafenberg, Potsdam 14473, Germany*

[4]*University of Nevada Las Vegas, Las Vegas, Nevada 89154, USA*

Abstract

A significant characteristic distinguishing Carlin-type Au deposits from other Au deposits is the abundance of invisible Au in arsenian pyrite. Gold occurs primarily as ionic Au^{1+} in arsenian pyrite and is unstable during subsequent thermal events. In this study, we used the focused ion beam combined with scanning electron microscope (FIB-SEM) techniques, and a transmission electron microscope (TEM) to examine invisible Au and how it evolved through later geologic events that eventually led to the formation of Au nanoparticles. FIB-SEM techniques were used to prepare site-specific TEM foils from four Carlin-type gold deposits, including Getchell and Cortez Hills, Nevada, USA, and Shuiyindong and Jinfeng, Guizhou Province, China. These samples were analyzed to quantify ore pyrite chemistry and evaluate textures at the nanometer scale.

In 17 examined TEM foils, we observed widespread Au-rich domains in high-grade Au arsenian pyrites from the Getchell and Cortez Hills Au deposits and the Jinfeng deposit but only 10 Au-bearing nanoparticles, ~10 to 20 nm in diameter. The Au-rich domains exhibit Au (Sb), (Tl), (Hg), and (Cu) peaks in the energy dispersive X-ray (EDX) spectrum without the presence of recognizable nanoparticles. This confirms that Au is invisible even at a nanometer scale and is most likely present in the crystal structure of arsenian pyrite. Stacking faults and nanometer-sized fluid inclusions were commonly observed in Au-bearing arsenian pyrite from the four deposits, implying rapid crystallization. Moreover, unlike the coarsely crystalline arsenian pyrite from Guizhou Carlin-type Au deposits, arsenian pyrite from Carlin-type deposits in Nevada consists of fine-grained poly-crystalline aggregates, further implying rapid crystallization. Additionally, curved dislocations were commonly pinned by solid inclusions, reflecting a former annealing process.

Combining nanoscale textures with geologic information previously reported for Carlin-type deposits, invisible ionic Au was initially incorporated into the crystal structure of arsenian pyrite during rapid precipitation. Subsequent post-ore magmatic events in both districts initiated the annealing of the ionic Au-bearing arsenian pyrite, leading to the redistribution of trace elements and formation of Au-bearing nanoparticles in the arsenian pyrite. The presence of predominantly ionically bonded Au in arsenian pyrite confirms that ore fluids were not saturated in Au when Au-bearing arsenian pyrite formed, as previously reported for Carlin-type deposits. Ionic Au that was scavenged from an undersaturated ore fluid and incorporated into the arsenian pyrite crystal structure formed the giant Carlin-type Au deposits.

Introduction

Gold is visible in most types of Au deposits as micrometer-sized grains of native Au or Au-Ag alloys (Goldfarb et al., 2005; Law and Phillips, 2005; Simmons, 2005). However, in Carlin-type Au deposits, which account for ~8% of annual worldwide Au production (Frimmel, 2008), Au is predominantly incorporated in arsenian pyrite and almost always invisible under the optical microscope and the scanning electron microscope (SEM) (Cline and Hofstra, 2000; Cline et al., 2005; Reich et al., 2005; Barker et al., 2009; Muntean et al., 2011; Su et al., 2018; Xie et al., 2018b), although, Au nanoparticles and even visible native Au have been observed in a few Carlin-type Au deposits (Bakken et al., 1989; Hochella, Jr., et al., 1998; Palenik et al., 2004; Deditius et al., 2011; Su et al., 2008, 2012). Knowledge of the deposition and evolution of invisible Au is the key to a better understanding of the genesis of these massive deposits.

Since Carlin-type Au deposits were recognized as a new deposit type in the 1980s, numerous analytical methods have

been used to investigate the chemical state of invisible Au. Several studies using X-ray photoelectron spectroscopy (XPS) (Fleet et al., 1993; Li et al., 1995; Maddox et al., 1998), X-ray absorption near edge structure (XANES) (Simon et al., 1999a; Cabri et al., 2000), and X-ray absorption fine structure (EX-AFS) (Simon et al., 1999b) indicate that invisible Au most likely exists as both Au^{1+} and Au^0 in arsenian pyrite, with Au^{1+} being dominant. These analyses further infer that Au^{1+} is structurally bound in a solid solution. Bakken et al. (1989) and Hochella, Jr., et al. (1998) used transmission electron microscope (TEM) to identify a few isolated Au nanoparticles in samples from the Nevada Carlin deposit. These particles were associated with pyrite, quartz, cinnabar, and illite. In addition, Palenik et al. (2004) observed large concentrations of Au nanoparticles in a high-grade arsenian pyrite sample from the Nevada Betze-Post deposit using a high-resolution TEM, which led them to suggest that Au^0 is present in significant abundance within nanoparticles in pyrite. However, because traditional TEM sample preparation techniques such as the tripod polishing or Argon ion milling method fail to prepare a site-specific TEM foil, the precise geochemistry of the TEM foil being analyzed was unknown, yielding problems in TEM data interpreta-

tion. Reich et al. (2005) and Deditius et al. (2014) compiled the Au and As contents of Au-bearing pyrite from numerous hydrothermal Au deposits, and these components plot in a wedge-shaped zone with an upper compositional limit defined by the line: $C_{Au} = (0.02) (C_{As}) + 4 \cdot 10^{-5}$. Combining this function with TEM observations, they predicted that Au in a solid solution is dominant in arsenian pyrite in Carlin-type Au deposits. Moreover, Gopon et al. (2019) recently used atom probe tomography to investigate the atomic-scale distribution of trace elements in a sample from the Turquoise Ridge Carlin-type deposit in the Getchell, Nevada, district. They did not observe Au nanonuggets and instead observed dispersed Au, which led them to suggest that Au occurs as diffuse atoms within arsenian pyrite. Furthermore, Reich et al. (2006), in an experimental study, directly observed small Au nanoparticles (~4 nm) that had begun to coarsen into larger particles above ~370°C and determined that Au nanoparticle would coarsen by Ostwald ripening. Metal remobilization in host minerals in response to post-ore metamorphism was also demonstrated by the observation of nanoparticle coarsening at a chromite deposit (González-Jiménez et al., 2015). In summary, previous studies determined that the invisible Au of Carlin-type deposits largely occurs as ionic Au^{1+} in arsenian pyrite, although Au nanoparticles were occasionally observed, and indicated that Au nanoparticles became unstable and coarsened during later thermal treatments.

Transmission electron microscopy allows us to observe microstructure and analyze the chemical composition of phases at the nanometer scale. Recent advances in TEM sample preparation techniques, especially the focused ion beam (FIB) combined with SEM, allow us to prepare a site-specific TEM foil from sample volumes in which the Au concentration has been precisely quantified by electron probe microanalysis (EPMA), laser ablation-inductively coupled plasma-mass spectrometry (LA-ICP-MS), or secondary ion mass spectrometry (SIMS) (Wirth, 2004; Wirth et al., 2009). This combination of SEM, FIB, and TEM techniques provides in situ chemical and microstructure analyses from the micrometer to the nanometer scale.

In this study, we utilized SEM-FIB techniques to prepare site-specific TEM foils. We present chemistry and microstructure data from four classic Carlin-type Au deposits, including two from the United States and two from China. Widespread Au-rich domains without Au nanoparticles were identified within Au-bearing arsenian pyrite at a nanometer scale, suggesting that invisible ionic Au in the studied Carlin-type deposits is most likely dominant in the arsenian pyrite crystal structure. A few Au-bearing nanoparticles in arsenian pyrite were observed. Nanoscale textures combined with geologic information suggest that these Au nanoparticles evolved from ionic Au in the arsenian pyrite during an annealing process associated with magmatic thermal events sometime after deposit formation.

Geologic Background

Key characteristics of Carlin-type deposits

The vast majority of Nevada Carlin-type Au deposits occur in four areas, including the Carlin, Cortez, and Getchell trends, and the Jerritt Canyon district (Hofstra and Cline, 2000; Cline et al., 2005; Muntean, 2018). These deposits remarkably share features that include the following:

1. Ore deposits are controlled by old, reactivated basement rift structures, and occur in clusters or are aligned along with these structures (Hofstra and Cline, 2000; Cline et al., 2005; Muntean et al., 2011; Muntean, 2018).
2. Orebodies are preferentially hosted by carbonate-bearing rocks and controlled by faults associated with a regional thrust (Cline et al., 2005; Muntean, 2018).
3. Au mineralization formed in response to water-rock reaction and was followed by post-ore orpiment, realgar, and lesser stibnite and calcite precipitation in open space as the system cooled and collapsed (Hofstra et al., 1991; Cline, 2001; Cline et al., 2005; Muntean et al., 2011).
4. The majority of Au is invisible and in arsenian pyrite, which is formed by sulfidation of Fe-bearing carbonate host rock (Muntean, 2018; Kusebauch et al., 2019). In addition to Au, the arsenian pyrite is enriched in Hg, Tl, Cu (Te), and Sb, with low to absent Ag and base metals (Simon et al., 1999b; Kesler et al., 2003; Reich et al., 2005; Barker et al., 2009; Maroun et al., 2017).
5. Hydrothermal alteration associated with auriferous pyrite precipitation includes both dissolution and silicification of carbonate minerals, and argillization of silicate minerals in the host rocks to form vuggy open space/jasperoid and clay minerals, respectively (Hofstra and Cline, 2000; Cail and Cline, 2001; Cline, 2001; Cline et al., 2005; Muntean, 2018).
6. The deposits generally formed at depths of less than ~3 km and at temperatures of 180° to 240°C, from moderately acidic (pH ≤5), reduced, and non-boiling fluids (Cline and Hofstra, 2000; Hofstra and Cline, 2000; Cline, 2001; Lubben et al., 2012).
7. The deposits formed from ~42 to 34 Ma, coincident with a southwest-trending magmatic event. Subsequent to Au deposition, explosive bimodal volcanism accompanied basin extension and faulting in the Great Basin, with some volcanism within or near the Au deposits (Hofstra and Cline, 2000; Cline et al., 2005; Ressel and Henry, 2006; Muntean et al., 2011).

Guizhou Carlin-type Au deposits share many characteristics with Nevada deposits, including tectonic setting, Au mineralization controlled by lithology and structure, invisible Au in arsenian pyrite, ore-stage minerals including quartz and illite, and late ore-stage sulfosalt minerals (Cline et al., 2013; Su et al., 2018; Xie et al., 2018a). Significantly, Guizhou ore pyrite rims are different from Nevada rims. The Guizhou rims are texturally identical to the pyrite cores and are not visible under a petrographic microscope. The pyrites are commonly subhedral to euhedral and contain significantly less Au, As, Hg, Tl, Cu, and Sb than Nevada ore pyrite (Xie et al., 2018a).

Another similarity is the occurrence of magmatism accompanying basin extension subsequent to Au mineralization, with some of the magmatism spatially related to Au deposits, although extension and magmatism in the Youjiang Basin, China, were much weaker compared with the Great Basin, USA (Xie et al., 2018a). Despite the similarities, Guizhou deposits formed at higher pressure, temperature, and pH conditions compared

with Nevada deposits, which resulted in less intense decarbonatization, silicification, and argillization (Xie et al., 2018a).

In this study, we focus on the Getchell and Cortez Hills deposits in Nevada, USA, and the Shuiyindong and Jinfeng deposits in Guizhou Province, China. The two Nevada deposits have characteristics typical of Nevada Carlin-type deposits described above. The stratabound Shuiyindong deposit is the largest Carlin-type Au deposit in China, with proven and probable Au reserves of 294 tonnes (t). The Jinfeng deposit is a typical fault-controlled Carlin-type deposit, with Au resources of 109 t. These two deposits are representative of Guizhou Carlin-type deposits (Xie et al., 2018a).

Sample selection and descriptions

Prior to TEM foil preparation, we quantified pyrite chemistry using EPMA and LA-ICP-MS (Xie et al., 2018a, 2018b) and then selected medium- and high-grade Au areas (82–5,318 ppm Au) for TEM analysis. Seventeen site-specific TEM foils from the four deposits were prepared (Table A1). Appendix Figures A1, A2, and A3 show the precise locations of the TEM foils in arsenian pyrites.

Briefly, Au-bearing arsenian pyrite from Guizhou deposits typically forms 1- to 30-µm-thick rims on pre-ore pyrites (Fig. 1A) or occurs as individual pyrite crystals with high relief, bright reflectivity, and a good polish (Fig. 1A; Figs. A1, A2A-C). This pyrite does not display the low relief and fuzzy texture typical of Au-bearing arsenian pyrite from Nevada deposits (Fig. 1B; Figs. A3A, B).

Arsenian pyrite from Guizhou deposits contains < ~130 ppm (EPMA detection limit) to 2,180 ppm Au, ~0.4 to 8.3 wt % As, ~316 to 3,190 ppm Cu, ~32 to 2,130 ppm Sb, <~56 ppm (EPMA detection limit) to 1,232 ppm Hg, <~4 ppm (LA-ICP-MS detection limit) to 690 ppm Tl, and ~21 to 50 ppm Pb (Tables A2, A3). In contrast, arsenian pyrite from Nevada contains higher concentrations of these elements: 1,350 to 5,318 ppm Au, ~1.5 to 10.6 wt % As, ~2,134 to 15,754 ppm Cu, ~284 to 7,617 ppm Sb, ~908 to 5,134 ppm Hg, ~9,290 to 37,378 ppm Tl, and ~94 to 665 ppm Pb (Appendix Tables A2, A3). Note that although arsenian pyrites from both Guizhou and Nevada are enriched in these elements, no visible particles of

these elements were observed using optical microscopy and SEM analyses in this study. Gold and As concentrations in the ore-stage arsenian pyrite from the four deposits all plot below the solubility limit defined by Reich et al. (2005) (Fig. 2).

Methods

Site-specific TEM foil preparation

The FIB technique combined with SEM imaging was used for site-specific TEM foil preparation at the Institute of Geochemistry, Chinese Academy of Sciences (IGCAS), and the German Research Centre for Geosciences (GFZ). Figure 3 shows the steps in the preparation of a site-specific TEM foil. First, we select medium- and high-grade sample sites for the site-specific TEM foil (Fig. 3A). We then cut TEM foil from the target area using FIB (Fig. 3B), removed the foil from its excavation site (Fig. 3B, C), and mounted the foil on the Cu- or Mo-grid (Fig. 3D). Commonly, the Mo-grid was used so that we could track changes in the Cu content of our samples. A typical foil has a dimension of ~12 × 10 × ~0.06 µm (Fig. 3D).

TEM analysis

The FEI Tecnai G2 F20 TEMs at the IGCAS, GFZ, and Nanjing University (NJU) were used for measuring pyrite chemistry and microstructure investigation at the nanometer scale. Both TEMs are equipped with a field emission gun as an electron source, a Gatan imaging filter GIF™, an EDAX X-ray analyzer (at IGCAS), or OXFORD X-Max^N (at NJU) with an ultrathin window and a Fischione high-angle annular dark-field (HAADF) detector. The HAADF images were acquired using a camera length of 75 mm, which avoids collecting Bragg scattered electrons. Bright-field, dark-field, and high-resolution TEM images were acquired as energy-filtered images, applying a 20-eV window to the zero-loss peak of the electron energy loss spectrum. Energy dispersive X-ray (EDX) analysis was performed with the TEM in scanning transmission (STEM) mode. The foil was tilted ~15° toward the detector prior to analytical electron microscopy data acquisition. The acquisition time was 120 to 240 seconds. Low GaK and GaL X-ray intensities in the spectra are due to Ga
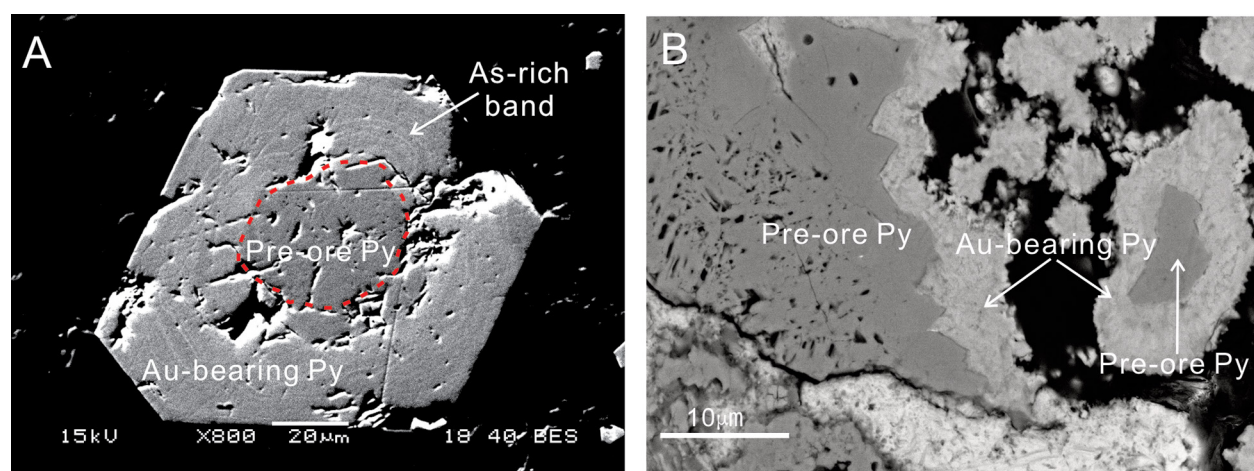

Fig. 1. Backscattered electron (BSE) images showing Au-bearing arsenian pyrite rimming pre-ore pyrite at Jinfeng, China (A) and Getchell, USA (B). A. Gold-bearing arsenian pyrite from the Jinfeng deposit exhibits narrow, bright oscillatory As-rich sub-bands. B. Getchell Au-bearing arsenian pyrite has irregular fuzzy rims. Py = pyrite.
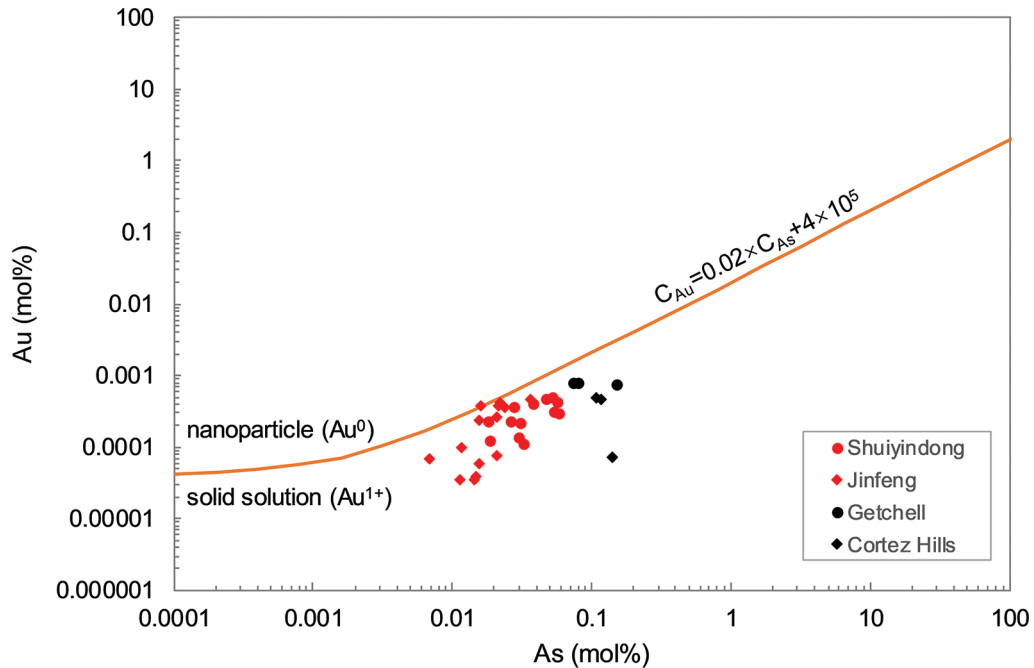
Fig. 2. The plot of Au-As EPMA analyses of ore-stage arsenian pyrite from Guizhou Shuiyindong and Jinfeng deposits, and Nevada Getchell and Cortez Hills deposits (log-scale, in mol %, the data sources are listed in Table A2). All analyses plot below the solubility limit, after Reich et al. (2005).
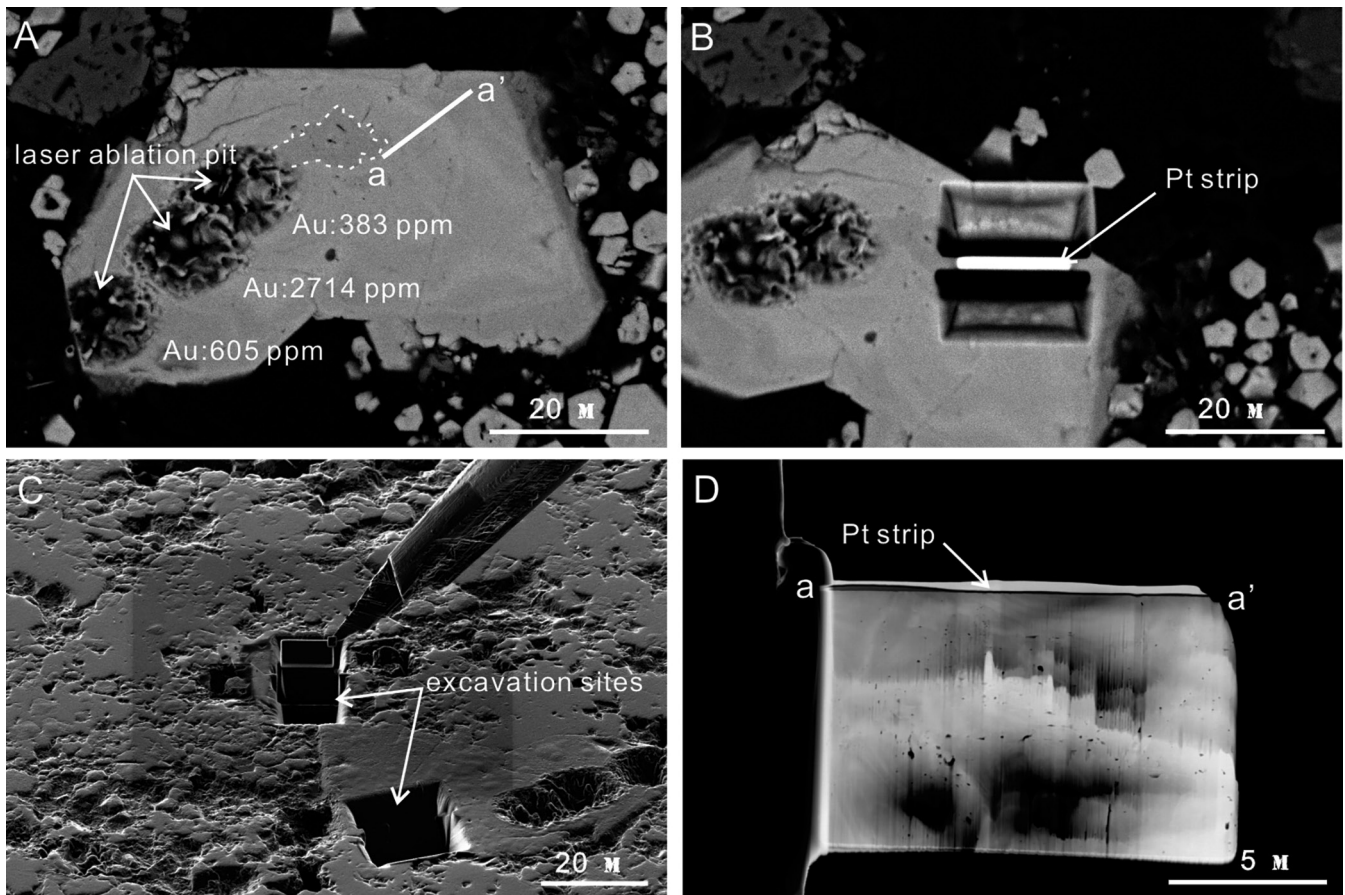

Fig. 3. Process of site-specific TEM foil preparation. (A) First, select the target area for TEM foil (marked with Line a-a′), (B) then cut the target area, (C) remove the foil from its excavation site, and (D) mount it onto the Mo-grid.

ion implantation during TEM foil preparation. The detection limit of EDX for Au is ~0.08 at % (~0.2 wt %) according to Wirth et al. (2013).

Results

Gold-rich domains in arsenian pyrites

Nanoscale Au-rich domains were observed in high-grade arsenian pyrites from Getchell and Cortez Hills, Nevada, and Jinfeng, China (Table 1). These domains are characterized by a weak Au*L* line at 9.7 keV in the EDX spectrum (Fig. 4B), and no nanoparticles have been observed at the nanometer scale in the HAADF image (Fig. 4A). In addition to Au, the domain occasionally contains detectable Sb, Tl, Hg, and Cu. Commonly, the Au-rich domains exhibit no significant difference in appearance from the matrix where Au is below the EDX detection limit, ~0.2 wt %, in HAADF imaging (Fig. 4C).

In the Getchell pyrite sample, an Au-rich domain larger than 34 µm² is indicated by up to 16 EDX spot analyses across high-grade (~5,318 ppm Au) arsenian pyrite. The EDX spectrum shows peaks for Au, Sb, Tl, and Hg but shows no visible nanoparticles at the location of the analysis (Fig. 4A, B; Table 1). In the Cortez Hills high-grade arsenian pyrite (~1,990 ppm Au), the Au-rich domain is a porous band with an area of ~0.06 µm² (Fig. A4A; Table 1). In this arsenian pyrite, the Au-rich domain is slightly brighter in the HAADF image than the matrix in which Au is below the EDX detection limit. The increased brightness might be a result of a higher concentration of As in this Au-rich domain.

High-grade Jinfeng arsenian pyrite contains up to 2,180 ppm Au and has an Au-rich domain larger than 0.16 µm² (right half side of Fig. 4C; Table 1) where both Au and Sb are detectable by EDX analyses. Gold-rich domains were not identified in the Shuiyindong arsenian pyrite and the Jinfeng medium-grade arsenian pyrite because Au concentrations were below the EDX detection limit.

Nanoparticles of Au-bearing and sulfophilic elements

Ten Au-bearing nanoparticles in arsenian pyrite were identified in 17 TEM foils from the four deposits (Table 2). These Au-bearing nanoparticles have a darker contrast in the bright field (BF) image (Fig. 5A) and a brighter contrast in the HAADF image (Fig. 5B) compared to the arsenian pyrite matrix. Two Au-bearing nanoparticles displaying characteristic Au*L* X-ray intensity (9.7 keV) and without distinguishable peaks of other elements, suggesting they are Au-only nanoparticles, were identified in Shuiyindong high-grade arsenian pyrite (~1,960 ppm Au). One particle, ~10 nm in diameter (Fig. 5A), is spherical, and the other nanoparticle, ~15 nm in diameter, is anhedral. Other Au-bearing nanoparticles in arsenian pyrite have a diameter of ~10 to 20 nm and exhibit Au*L* peaks and also peaks of Sn (Shuiyindong), Sb-Hg (Jinfeng), Sb-(Tl)-(Hg) (Getchell), and Tl-(Sb)-(Cu) (Cortez Hills) in the EDX spectrum (Table 2). The Au concentration of the surrounding matrix at the four studied deposits is below the EDX detection limit.

Minor sulfophilic-element nanoparticles with Au below detection were also identified in arsenian pyrite from the four deposits (Table A4). They are commonly 10 to 50 nm in diameter, locally up to 100 nm in diameter, and anhedral in shape. Among these nanoparticles Cu-, Sb-, Pb-, and Hg-bearing nanoparticles are the most common. This is consistent with high concentrations of these elements in arsenian pyrite from EPMA measurements (Table A2) and/or LA-ICP-MS (Table A3). Thallium-Cu-(Hg)-(S) nanoparticles occur only in arsenian pyrite from Nevada deposits possibly because of relatively higher Tl, Cu, and Hg concentrations (Tables A2, A3).

Crystallization and crystal defects in arsenian pyrite

Arsenian pyrite from Guizhou deposits is coarsely crystalline and exhibits oscillatory As zoning parallel to the growth surface (Fig. 1A; Fig. A4D). In contrast, arsenian pyrite from Nevada deposits exhibits a fine-grained polycrystalline aggregate, and individual microcrystals have widths of ~50 to 250 nm and lengths of ~1 to 1.5 µm (Fig. 6B). Arsenian pyrite rims at Getchell consist of two zones (Fig. 6A) with the outer zone exhibiting an irregular, fuzzy crystal surface (Fig. 6A).

Dislocations are common in the Au-bearing arsenian pyrite, especially in a sample from the Jinfeng deposit. The dislocation lines are ~100 to 200 nm in length, and are curved, with trace element-rich nanoparticles at the turning site (Fig. 7D). These trace element-bearing nanoparticles have pinned the dislocations during their movement by dislocation climb, which is a thermally activated process and suggests annealing at an elevated temperature during post-ore events.

Stacking faults occur as thin narrow platelike features in TEM BF and HAADF images (Fig. 7A-D). Note how the stacking fault (Fig. 7B) offsets microtextures visible in Figure 7A. Streaks in fast Fourier transform (FFT) diffraction patterns from HRTEM images further confirm the stacking faults (Fig. 7B). These faults have a width of ~3 to 8 nm and lengths of ~500 to 1,000 nm and are typically parallel to the (100) or (200) lattice planes of the arsenian pyrite (Fig. 7B-C). The stacking faults are commonly terminated by fluid inclusions (Fig. 7A). Some amorphous nanoparticles, such as a Pb-S nanoparticle, are hosted in the stacking faults (Fig. 7C).

Nanometer-sized fluid inclusions (~50 nm in diameter) are commonly observed, especially in Jinfeng high-grade arsenian pyrite. Fluid inclusions are darker than the arsenian pyrite matrix in HAADF images (right half of Fig. 4C). Some fluid inclusions are elongated, with the long axis parallel to the stacking

Table 1. Gold-Rich Domain in Arsenian Pyrite Confirmed by TEM-EDS Analysis

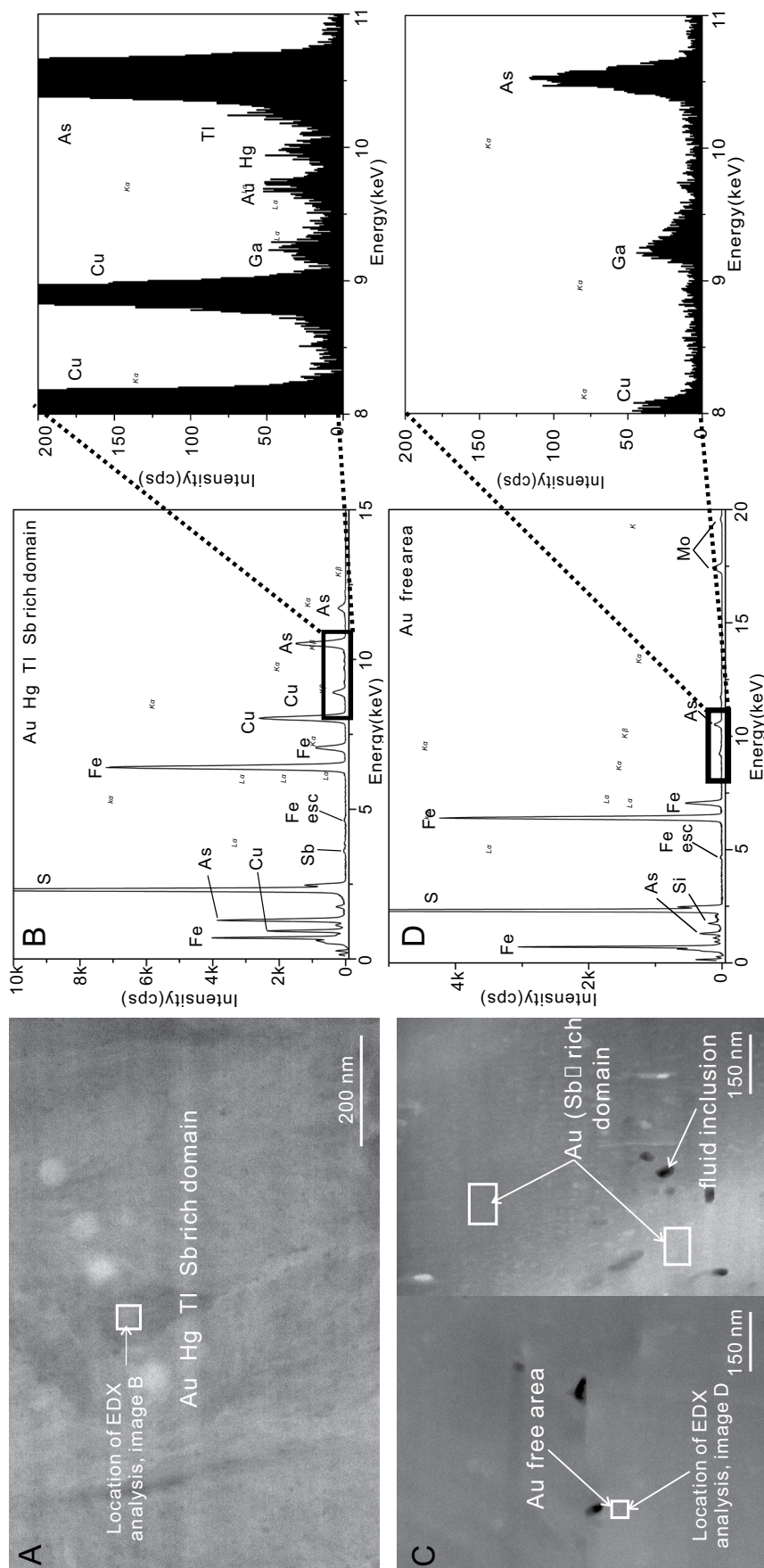| Deposit	Foil number	Gold-rich domain	Area (µm²)	Note
Jinfeng	HDDS-0154B-767A	Au-(Sb)	> 0.06	The boundary was not defined
Getchell	GZ-16-14-A1	Au-Sb-Tl-Hg	~34	The entire area of arsenian pyrite in this foil contains Au above the detection limit of EDX
Cortez Hills	DC-215-1423A	Au	~0.16	The Au-rich domain is a porous band

Fig. 4. High-angle annular dark-field (HAADF) images (A, C) and energy-dispersive X-ray spectroscopy (EDX) spectrum (B, D) of the Au-rich domain and Au-free (below detection limit) area in Au-bearing pyrite. A. A gold-rich domain in Au-bearing arsenian pyrite from the Getchell deposit has no visible nanoparticles, but (B) exhibits Au, As, Hg, Tl, Cu, and Sb peaks in the EDX spectrum. White spots on image A are a result of carbon contamination by the electron beam during EDX analysis. C. An Au-free area and Au-rich domain in Au-bearing arsenian pyrite from the Jinfeng deposit show no visible nanoparticles. The brighter band on the right side of "C" is probably a result of Ga implantation during TEM foil preparation. D. An EDX spectrum of the Au-free area shows the Au concentration in the arsenian pyrite is below the EDX detection limit. The Mo peak in the EDX spectrum (D) is from the Mo grid on which the sample rests.

fault (Fig. A4B). Locally, the fluid inclusions contain Pb-Ni-Cu-(Zn)-(Sb)-(Bi)-(Hg)-(Sn)-(S) nanoparticles (Fig. A4C).

Discussion

Although a few Au-bearing nanoparticles were observed, widespread Au-rich domains of high-grade Au arsenian pyrites indicate that nearly all Au in arsenian pyrite is invisible even at a nanometer scale. We suggest that invisible Au was primarily incorporated into the crystal structure of arsenian pyrite, although the presence of some near atomic-scale clusters of Au^0 cannot be completely ruled out. This is consistent with the plotting of Au and As concentrations in the arsenian pyrite (Fig. 2), which also suggests that Au is present in a solid solution. Additionally, our TEM observations are consistent with previous studies using Mössbauer spectroscopy (Friedl et al., 1995; Genkin et al., 1998), EXAFS (Simon et al., 1999a), and XPS techniques (Maddox et al., 1998), which infer that most invisible Au in the Guizhou and Nevada Carlin-type deposits is incorporated in the arsenian pyrite crystal structure as Au^{1+}. Furthermore, our TEM results suggest that Au-rich domains

Table 2. Gold and Au-Bearing Nanoparticles in Arsenian Pyrite Confirmed by TEM-EDS Analysis

Deposit	Foil number	Nanoparticle	Size (diameter, nm)
Shuiyindong	SYD17-2-7	Au-Sn-(S)	~10
		Au	~10
		Au	~15
Jinfeng	HDDS-0154B-767A	Au-Sb-Hg-(S)	~10
		Au-Sb-Hg-(S)	~20
Getchell	GZ-16-14-A1	Au-Sb-Tl-Hg-(S)	~20
		Au-Sb-(S)	~20
Cortez Hills	DC-215-1423B	Au-Tl-(S)	~10
		Au-Cu-Sb-Tl-(S)	~10
		Au-Tl-(S)	~10

Note that owing to abundant S in the pyrite matrix, S abundance in the nanoparticle is uncertain

in arsenian pyrite are heterogeneously distributed at a nanometer scale. This variability of Au in pyrite could have been caused by locally variable Au concentrations in the ore fluid when the Au-bearing arsenian pyrite precipitated.
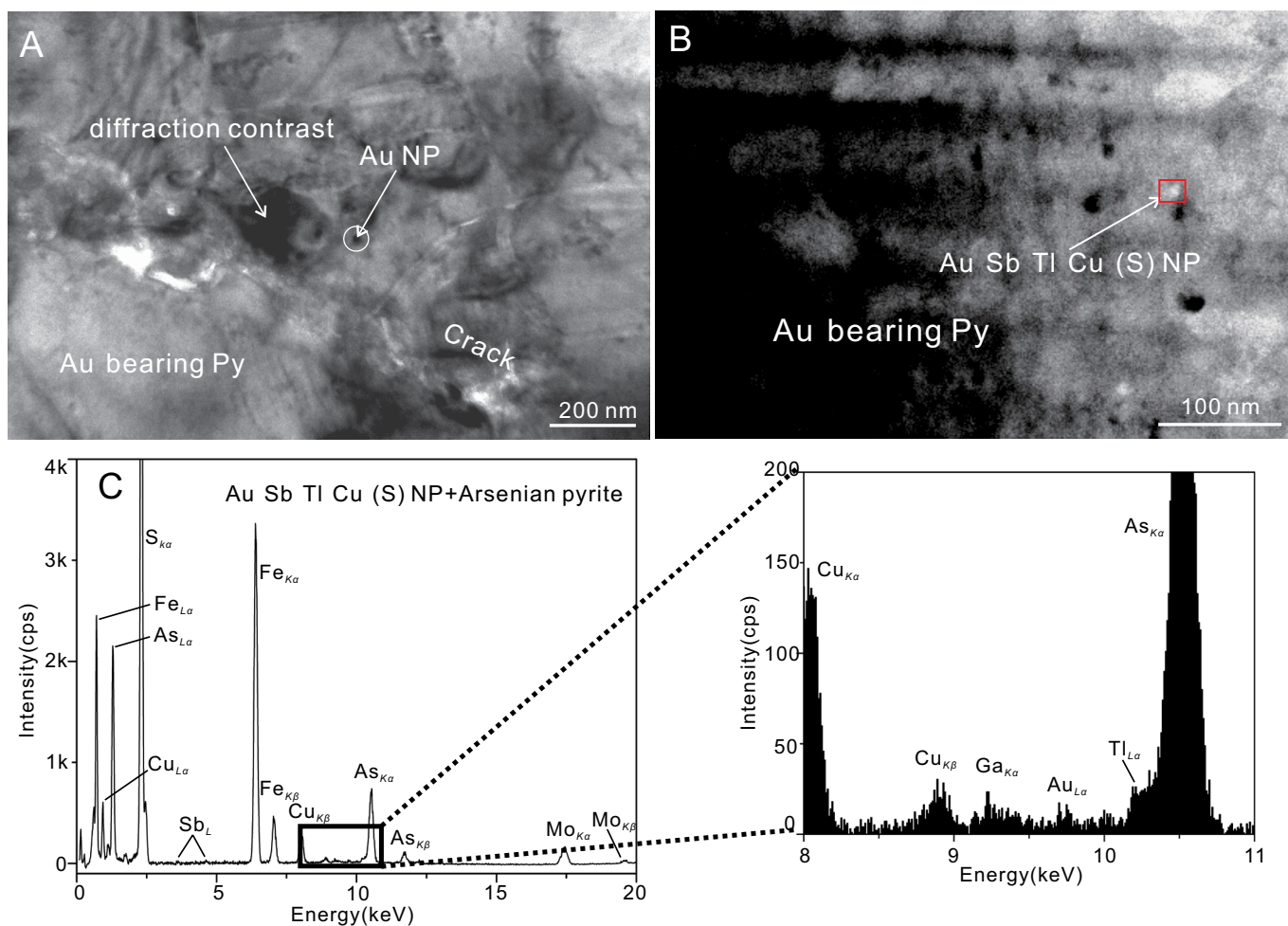

Fig. 5. An Au nanoparticle in arsenian pyrite from the Shuiyindong deposit (A) and Au-bearing nanoparticle in arsenian pyrite from the Cortez Hills deposit (B, C). A. Bright field (BF) image shows an Au nanoparticle (dark spot) in arsenian pyrite. B. A high-angle annular dark-field (HAADF) image shows an Au-Sb-Tl-Cu-(S) nanoparticle, which is documented by peaks in the energy-dispersive X-ray spectroscopy (EDX) spectrum (C). The white circle and red rectangle in images A and B, respectively, indicate the spot size of EDX analyses. Abbreviations: NP = nanoparticle.
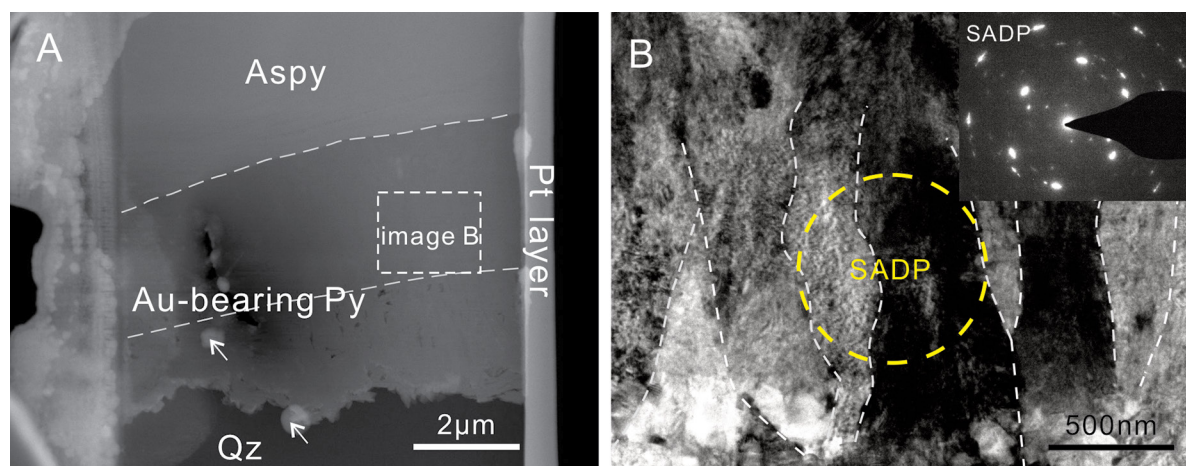
Fig. 6. High-angle annular dark-field (HAADF) image (A) and bright-field (BF) image (B) showing textures of Au-bearing arsenian pyrite from Getchell. A. The arsenian pyrite consists of two microcrystalline bands, with boundary indicated by the dashed line; the outer band exhibits an irregular fuzzy edge. The white spots on the image (arrows) are dust contamination during foil storage. B. The BF image shows the inner band consists of a polycrystalline aggregate, and the individual microcrystals are not equant. Selected area diffraction pattern (SADP) indicates that the crystals in the yellow cycle have strong preferred orientation relationships. They are slightly misoriented, which is documented by the smeared out strong reflections of pyrite. Abbreviations: Aspy = arsenopyrite, Py = pyrite, Qz = quartz.

Initial occurrence of invisible Au in arsenian pyrite

Growth stacking faults and nanometer-sized fluid inclusions are common in arsenian pyrite of the four deposits, especially in pyrite from the Jinfeng deposit, suggesting that arsenian pyrite is formed by rapid crystallization (Hannay and Girifalco, 1975). Additionally, unlike the China Carlin-type deposits, arsenian pyrite in the Nevada deposits is polycrystalline, and the individual microcrystals are not equant (Fig. 6B), further implying rapid crystallization (Hobbs et al., 1981; Drury and Urai, 1990). Thus, it is concluded that ore-stage arsenian pyrites in Guizhou and Nevada Carlin-type deposits formed during rapid crystallization.

Trace element incorporation into a mineral is, under equilibrium conditions, controlled by the element's partition coefficient (Kusebauch et al., 2018, 2019). Rapid crystallization indicates a nonequilibrium reaction between the mineral and the hydrothermal fluid and generally a nonequilibrium partition coefficient is larger than an equilibrium partition coefficient (Xu, 2000). In addition, several studies have demonstrated that a high As concentration in pyrite would significantly enhance the Au partition coefficient and promote Au partitioning into the pyrite (Reich et al., 2005; Chen et al., 2013; Kusebauch et al., 2019; Xing et al., 2019). Hence, more Au and trace elements would be incorporated into arsenian pyrite during rapid nonequilibrium crystallization.

In Carlin-type hydrothermal systems, Au is principally transported as or Au(HS)^0 in more acidic fluids (Seward, 1973; Stefánsson and Seward, 2004; Williams-Jones et al., 2009; Liu et al., 2014) and the Au-HS complexes were adsorbed onto the growing arsenian pyrite surface, which has a small negative charge (Widler and Seward, 2002). Two key characteristics of Carlin-type mineralization, including ore formation from water-rock interaction and a lack of evidence for ore fluid boiling (Cline and Hofstra, 2000; Hofstra and Cline, 2000; Cline et al., 2005; Su et al., 2009, 2018), are consistent with Au concentrations in the ore fluid below

saturation when pyrite precipitated. This is in agreement with a recent thermodynamic modelling and experimental study by Kusebauch et al. (2019), which also indicates that the ore fluid was undersaturated concerning native Au. Gold was most likely adsorbed onto the pyrite crystal structure from an undersaturated fluid. The experimental study (Kusebauch et al., 2019) and density functional theory calculations (Chen et al., 2013, 2014) suggest that Au was readily incorporated into interstitial lattice sites or at S^{-2} vacancy sites of arsenian pyrite where As substituted for S (Cook and Chryssoulis, 1990; Simon et al., 1999a; Savage et al., 2000). Our TEM analyses of Au-rich domains in arsenian pyrite and the rarity of Au-bearing nanoparticles are consistent with the presence of Au in the crystal structure of the arsenian pyrite as the primary state of Au in Carlin-type Au deposits, and this ionic Au most likely occurs as Au^{1+}(Simon et al., 1999a).

Formation of the Au-bearing nanoparticles

There are two possible scenarios for the origin of Au-bearing nanoparticles in Carlin-type ore deposits: (1) the Au concentration at the pyrite growth surface locally exceeded the Au solubility limit during arsenian pyrite crystallization, resulting in the crystallization of an Au particle, which was subsequently enclosed by the growing pyrite; or (2) the Au (and other heavy elements) in the metastable arsenian pyrite were redistributed during later geological events (Palenik et al., 2004; Reich et al., 2005; Deditius et al., 2011).

If the first mechanism for the formation of Au-bearing nanoparticles is correct, nanoparticles more likely would have formed in Au-rich domains. However, this is not what we observe. Additionally, the plotting of Au and As concentrations confirms an absence of Au nanoparticles (Fig. 2), which suggests that the ore fluid was undersaturated with respect to native Au (Reich et al., 2005; Deditius et al., 2011). This is consistent with a lack of geological or microstructural evidence showing Au saturation in the ore fluids.
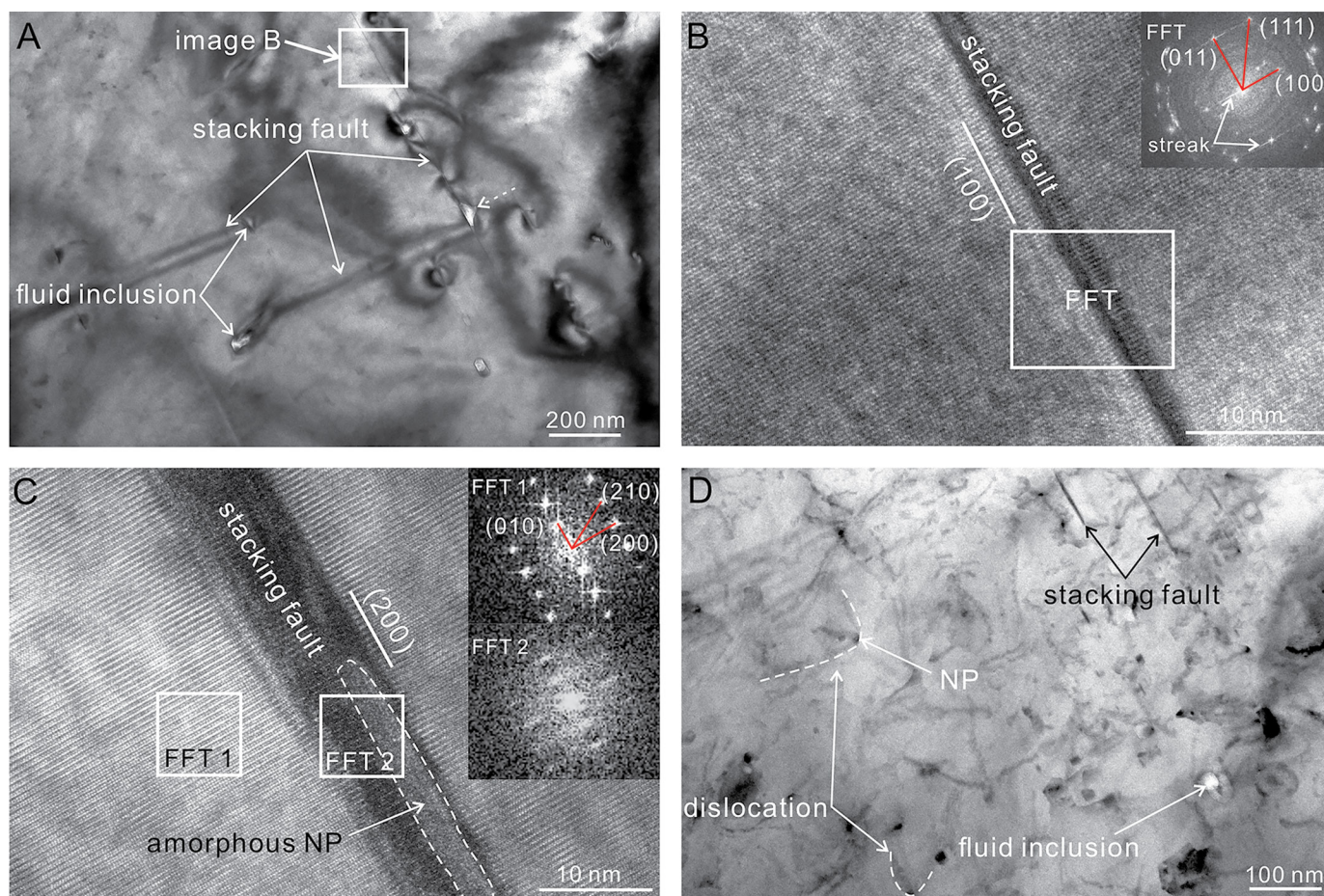
Fig. 7. Microstructures of Au-bearing arsenian pyrite from the Jinfeng deposit. A. A bright-field (BF) image shows stacking faults that highlight planar defects and associated fluid inclusions in Au-bearing arsenian pyrite. The endpoint of the stacking fault is usually decorated by a fluid inclusion. B. A high-resolution transmission electron microscopy (HRTEM) image shows a stacking fault parallel to the (100) plane of arsenian pyrite. The inserted image is the fast Fourier transform (FFT) image from the white rectangular area. FFT was indexed as arsenian pyrite. C. An HRTEM image shows a stacking fault parallel to the (200) plane of arsenian pyrite and an amorphous nanoparticle in the stacking fault. The FFT image from area 2 (FFT 2) shows streaking of the diffraction spots caused by the very thin plane of the stacking fault. The FFT from area 1 (FFT 1) indicates crystalline pyrite. D. A BF image shows dislocations and stacking faults in Au-bearing pyrite. Some dislocations that bend around a nanoparticle are highlighted by white dashed lines. NP = nanoparticle.

Our results favor the second mechanism of formation of Au-bearing nanoparticles that involves Au redistribution in Au-rich metastable arsenian pyrite due to annealing. An experimental study by Reich et al. (2006) determined that heating would lead to remobilization of invisible Au and formation and coarsening of Au nanoparticles. This interpretation is further supported by demonstrated coarsening of mantle Ru-Os-Ir nanoparticles interpreted as related to later thermal metamorphism (González-Jiménez et al., 2015). The annealing process resulted from a heating treatment during which crystalline materials lower their free energy by reducing defects in the crystal structure (Hummel, 2004; Shackelford, 2016).

Generally, dislocations form during deformation, but they also form during crystal growth as growth defects (Putnis, 1992; Hirth and Kubin, 2010). To reduce the free energy of the crystal, the dislocations will migrate into grain or phase boundaries or crystal surfaces during later thermal annealing by dislocation climb (Hobbs et al., 1981; Vukmanovic et al., 2014; Shackelford, 2016; Dubosq et al., 2018). Such a process

could have been recorded by ore-stage pyrite. In our observation, dislocations are curved and commonly pinned by solid inclusions. This suggests that dislocations were mobile during dislocation climb, which is a thermally activated process and indicates annealing (Putnis, 1992; Pettifor, 1996; Panigrahi and Jayaganthan, 2010; Hull and Bacon, 2011). During the recovery stage of the annealing, the migrating dislocations concentrate heavy elements such as Au and other sulfophilic elements at grain boundaries (Hobbs et al., 1981; Vukmanovic et al., 2014; Shackelford, 2016; Dubosq et al., 2018). During later recrystallization, while annealing at higher temperatures, arsenian pyrite recrystallized to equant polycrystals, and the migrating grain boundaries acted as a sink for heavy elements and commonly formed nanoparticles (Smith, 1964; Lawrence, 1972; McClay and Ellis, 1983; Yoon et al., 2002; Panigrahi and Jayaganthan, 2010; Dubosq et al., 2018).

In general, two possibilities—including later magmatic-thermal and compressive tectonic-thermal events—provide heat-initiating thermal annealing of pyrite. In both Nevada

and Guizhou districts, there are no compressive tectonic events subsequent to Au mineralization (Hofstra and Cline, 2000; Cline et al., 2005; Xie et al., 2018a). Additionally, the pyrites in both districts did not record any textures related to post-ore tectonism, such as pressure shadow and brittle deformation structures. Thus, we do not favor a compressive tectonic-thermal model. Instead, post-ore magmatism, some associated with basin extension, did occur within or near the four studied deposits. For example, post-ore bimodal volcanism (~15 Ma) occurred 3 to 4 km from the Cortez Hills deposit (Arbonies et al., 2011), and ~41 Ma post-ore rhyolite and dacite lavas and tuffs crop out within ~6 km of the Getchell deposit (Ressel and Henry, 2006). Post-ore alkaline ultramafic dikes (88 –85 Ma) are present ~20 km from the Shuiyindong and Jinfeng deposits (Liu et al., 2010). Additionally, Huang et al. (2019) identified evidence for a post-ore thermal event of ~88 Ma corresponding to alkaline ultramafic magmatism at the Shuiyindong deposit using zircon fission-track analyses. The temperature of this thermal event is estimated as ~170° to 200°C, approximately equal to the sealing temperature of zircon fission-tracks. This heat would have initiated annealing of arsenian pyrite because of the abundant low melting-point chalcophile elements such as Hg, Sb, Te, and Bi in arsenian pyrite that would have depressed its melting temperature to below 300°C (Tomkins et al., 2004, 2007) and lowered the initial annealing temperature to below 200°C, about one-half to two-thirds of the initial melting temperature (Lawrence, 1972; Shackelford, 2016). For the two Nevada deposits, Miocene dikes occur near Cortez Hills, and ~41 Ma lavas are present near the Getchell deposit. Thus, magmatism could have triggered arsenian pyrite annealing.

Based on the described geology, we propose that the post-ore Late Cretaceous magmatism in the Youjiang Basin, China, and Eocene and Miocene magmatism in the Great Basin, USA, provided the heat that initiated arsenian pyrite annealing in the Guizhou and Nevada deposits, respectively. The observed Au-bearing nanoparticles in this and previous studies may have formed during the annealing process.

Conclusions and Implications

This study identified widespread, Au-rich domains in high-grade Au arsenian pyrites from the Getchell and Cortez Hills deposits in Nevada, and the Jingfeng deposit in Guizhou, and confirms that invisible Au was initially and principally incorporated into the crystal structure of arsenian pyrite during rapid crystallization (Reich et al., 2005; Kusebauch et al., 2018, 2019; Muntean, 2018). Post-ore thermal events related to post-ore magmatism in both Nevada and Guizhou Carlin-type districts-initiated annealing of ionic Au-bearing arsenian pyrite. This led to a redistribution of trace elements and ultimately the formation of Au-bearing nanoparticles in arsenian pyrite. We infer that the closer the post-ore magmatism was to the Au deposits, the more Au-bearing nanoparticles will be observed because a higher temperature would more likely have led to greater recrystallization of arsenian pyrite and formation of Au-bearing nanoparticles.

The presence of original ionic Au in arsenian pyrite confirms that Carlin-type ore fluids were not saturated in Au when Au-bearing arsenian pyrite formed. If Au saturation was required, only Au in excess of the Au solubility limit would have pre-cipitated, with potentially significant Au remaining in the ore fluids. Alternatively, Au deposition from undersaturated ore fluids resulted in the transfer of a tremendous amount of Au from the ore fluid to arsenian pyrite. Even though ore fluids were not highly enriched in Au, giant Carlin-type Au deposits formed because of the efficient mechanism of Au deposition. We support a model in which Au scavenging by arsenian pyrite and adsorption into the pyrite crystal structure from an undersaturated fluid is the key mechanism for the formation of giant Carlin-type Au deposits.

REFERENCES
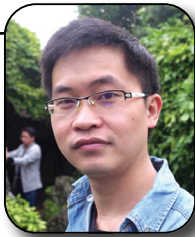
Arbonies, D.G., Creel, K.D., and Jackson, M.L., 2011, Cortez Hills lower zone discovery and geologic update, in Steininger, R.C., and Pennell, W.M., eds., Great Basin evolution and metallogeny: Geological Society of Nevada 2010 Symposium proceedings: Reno, Nevada, Geological Society of Nevada, p. 447–462.

Bakken, B.M., Hochella, M.F., Marshall, A.F., and Turner, A.M., 1989, High-resolution microscopy of gold in unoxidized ore from the Carlin mine, Nevada: Economic Geology, v. 84, p. 171–179.

Barker, S.L.L., Hickey, K.A., Cline, J.S., Dipple, G.M., Kilburn, M.R., Vaughan, J.R., and Longo, A.A., 2009, Uncloaking invisible gold: Use of nanosims to evaluate gold, trace elements, and sulfur isotopes in pyrite from Carlin-type gold deposits: Economic Geology, v. 104, p. 897–904.

Cabri, L.J., Newville, M., Gordon, R.A., Crozier, E.D., Sutton, S.R., McMahon, G., and Jiang, D.T., 2000, Chemical speciation of gold in arsenopyrite: Canadian Mineralogist, v. 38, p. 1265–1281.

Cail, T. and Cline, J.S., 2001, Alteration associated with gold mineralization at the Getchell Carlin-type gold deposit, northern Nevada, USA: Economic Geology, v. 96, p. 1343–1359.

Chen, J., Li, Y., and Zhao, C., 2014, First principles study of the occurrence of gold in pyrite: Computational Materials Science, v. 88, p. 1–6.

Chen, J., Li, Y., Zhong, S., and Guo, J., 2013, DFT simulation of the occurrences and correlation of gold and arsenic in pyrite: American Mineralogist, v. 98, p. 1765–1771.

Cline, J.S., 2001, Timing of gold and arsenic sulfide mineral deposition at the Getchell Carlin-type gold deposit, north-central Nevada: Economic Geology, v. 96, p. 75–90.

Cline, J.S., and Hofstra, A.A., 2000, Ore-fluid evolution at the Getchell Carlin-type gold deposit, Nevada, USA: European Journal of Mineralogy, v. 12, p. 195–212.

Cline, J.S., Hofstra, A.H., Muntean, J.L., Tosdal, R.M., and Hickey, K.A., 2005, Carlin-type gold deposits in Nevada: Critical geologic characteristics and viable models: Economic Geology 100th Anniversary Volume, p. 451–484.

Cline, J.S., Muntean, J.L., Xuexiang, G.U., and Xia, Y., 2013, A comparison of Carlin-type gold deposits: Guizhou Province, Golden Triangle, southwest China, and northern Nevada, USA: Geoscience Frontiers, v. 20, p. 1–18.

Cook, N.J., and Chryssoulis, S.L., 1990, Concentrations of invisible gold in the common sulfides: Canadian Mineralogist, v. 28, p. 1–16.

Deditius, A.P., Utsunomiya, S., Reich, M., Kesler, S.E., Ewing, R.C., Hough, R., and Walshe, J., 2011, Trace metal nanoparticles in pyrite: Ore Geology Reviews, v. 42, p. 32–46.

Deditius, A.P., Reich, M., Kesler, S.E., Utsunomiya, S., Chryssoulis, S.L., Walshe, J., and Ewing, R.C., 2014, The coupled geochemistry of Au and As in pyrite from hydrothermal ore deposits: Geochimica et Cosmochimica Acta, v. 140, p. 644–670.

Drury, M.R., and Urai, J.L., 1990, Deformation-related recrystallization processes: Tectonophysics, v. 172, p. 235–253.

Dubosq, R., Lawley, C.J.M., Rogowitz, A., Schneider, D.A., and Jackson, S., 2018, Pyrite deformation and connections to gold mobility: Insight from microstructural analysis and trace element mapping: Lithos, v. 310–311, p. 86–104.

Fleet, M.E., Chryssoulis, S.L., Davidson, R., Weisener, C.G., and Maclean, P.J., 1993, Arsenian pyrite from gold deposits: Au and As distribution investigated by SIMS and EMP, and color staining and surface oxidation by XPS and LIMS: Canadian Mineralogist, v. 31, p. 1–17.

Friedl, J., Wagner, F., and Wang, N., 1995, On the chemical-state of combined gold in sulfidic ores-conclusions from mossbauer source experiments: Neues Jahrbuch Fur Mineralogie-Abhandlungen, v. 169, p. 279–290.

Frimmel, H.E., 2008, Earth's continental crustal gold endowment: Earth and Planetary Science Letters, v. 267, p. 45–55.

Genkin, A.D., Bortnikov, N.S., Cabri, L.J., Wagner, F., Stanley, C.J., Safonov, Y.G., McMahon, G., Friedl, J., Kerzin, A.L., and Gamyanin, G.N., 1998, A multidisciplinary study of invisible gold in arsenopyrite from four mesothermal gold deposits in Siberia, Russian Federation: Economic Geology, v. 93, p. 463–487.

Goldfarb, R., Baker, T., Dube, B., Groves, D.I., Hart, C.J., and Gosselin, P., 2005, Distribution, character and genesis of gold deposits in metamorphic terranes: Economic Geology 100th Anniversary Volume, p. 451–484.

González-Jiménez, J.M., Reich, M., Camprubí, A., Gervilla, F., Griffin, W.L., Colás, V., O'Reilly, S.Y., Proenza, J.A., Pearson, N.J., and Centeno-García, E., 2015, Thermal metamorphism of mantle chromites and the stability of noble-metal nanoparticles: Contributions to Mineralogy and Petrology, v. 170, 15 p.

Gopon, P., Douglas, J.O., Auger, M.A., Hansen, L., Wade, J., Cline, J.S., Robb, L.J., and Moody, M.P., 2019, A nanoscale investigation of Carlin-type gold deposits: An atom-scale elemental and isotopic perspective: Economic Geology, v. 114, p. 1123–1133.

Hannay, N., and Girifalco, L., 1975, Treatise on solid state chemistry vol. 1: The chemical structure of solids: New York, Plenum Press, 549 p.

Hirth, J.P., and Kubin, L., 2010, Dislocations in solids: Amsterdam, Elsevier, 282 p.

Hobbs, B.E., Etheridge, M.A., and Cox, S.F., 1981, The experimental ductile deformation of polycrystalline and single crystal pyrite: Economic Geology, v. 76, p. 2105–2117.

Hochella, Jr., M., Rakovan, J., Rosso, K., Bickmore, B., and Rufe, E., 1998, New directions in mineral surface geochemical research using scanning probe microscopes, *in* Sparks, D.L., and Grundl, T.J., eds., Mineral-water interfacial reactions: Washington, ACS Publications, p. 37–56.

Hofstra, A.H., and Cline, J.S., 2000, Characteristics and models for Carlin-type gold deposits: Reviews in Economic Geology, p. 163–220.

Hofstra, A.H., Leventhal, J.S., Northrop, H.R., Landis, G.P., Rye, R.O., Birak, D.J., and Dahl, A.R., 1991, Genesis of sediment-hosted disseminated-gold deposits by fluid mixing and sulfidization: Chemical–reaction–path modeling of ore-depositional processes documented in the Jerritt Canyon district, Nevada: Geology, v. 19, p. 36–40.

Huang, Y., Hu, R., Bi, X., Fu, S., Peng, K., Gao, W., Oyebamiji, A., and Zhaanbaeva, A., 2019, Low-temperature thermochronology of the Carlin-type gold deposits in southwestern Guizhou, China: Implications for mineralization age and geological thermal events: Ore Geology Reviews, no. 103178, doi.org/10.1016/j.oregeorev.2019.103178.

Hull, D., and Bacon, D.J., 2011, Introduction to dislocations: Oxford, Elsevier, 268 p.

Kesler, S.E., Fortuna, J., Ye, Z., Alt, J.C., Core, D.P., Zohar, P., Borhauer, J., and Chryssoulis, S.L., 2003, Evaluation of the role of sulfidation in deposition of gold, Screamer section of the Betze-Post Carlin-type deposit, Nevada: Economic Geology, v. 98, p. 1137–1157.

Kusebauch, C., Oelze, M., and Gleeson, S.A., 2018, Partitioning of arsenic between hydrothermal fluid and pyrite during experimental siderite replacement: Chemical Geology, v. 500, p. 136–147.

Kusebauch, C., Gleeson, S., and Oelze, M., 2019, Coupled partitioning of Au and As into pyrite controls formation of giant Au deposits: Science Advances, v. 5, p. 1–8.

Law, J., and Phillips, G., 2005, Hydrothermal replacement model for Witwatersrand gold: Economic Geology 100th Anniversary Volume, p. 799–812.

Lawrence, L.J., 1972, The thermal metamorphism of a pyritic sulfide ore: Economic Geology. v. 67, p. 487–496.

Li, J., Fang, D., Qi, F., and Zhang, G., 1995, The existence of the negative charge of gold in sulphide minerals and its formation mechanism: Acta Geologica Sinica (English Edition), v. 8, p. 303–315.

Liu, S., Su, W.C., Hu, R.Z., Feng, C.X., Gao, S., Coulson, I.M., Wang, T., Feng, G.Y., Tao, Y., and Xia, Y., 2010, Geochronological and geochemical constraints on the petrogenesis of alkaline ultramafic dykes from southwest Guizhou Province, SW China: Lithos, v. 114, p. 253–264.

Liu, W., Etschmann, B., Testemale, D., Hazemann, J.L., Rempel, K., Müller, H., and Brugger, J., 2014, Gold transport in hydrothermal fluids: Competition among the Cl–, Br–, HS– and NH_3 (aq) ligands: Chemical Geology, v. 376, p. 11–19.

Lubben, J.D., Cline, J.S., and Barker, S.L.L., 2012, Ore fluid properties and sources from quartz associated with gold at the Betze-Post Carlin-type gold deposit, Nevada, United States: Economic Geology, v. 107, p. 1351–1385.

Maddox, L.M., Bancroft, G.M., Scaini, M.J., and Lorimer, J.W., 1998, Invisible gold: Comparison of Au deposition on pyrite and arsenopyrite: American Mineralogist, v. 83, p. 1240–1245.

Maroun, L.C., Cline, J.S., Simon, A., Anderson, P., and Muntean, J.L., 2017, High-grade gold deposition and collapse breccia formation, Cortez Hills Carlin-type gold deposit, Nevada, USA: Economic Geology, v. 112, p. 707–740.

McClay, K., and Ellis, P., 1983, Deformation and recrystallization of pyrite: Mineralogical Magazine, v. 47, p. 527–538.

Muntean, J.L., 2018, The Carlin gold system: Applications to exploration in Nevada and beyond: Reviews in Economic Geology, v. 20, p. 39–88.

Muntean, J.L., Cline, J.S., Simon, A.C., and Longo, A.A., 2011, Magmatic-hydrothermal origin of Nevada's Carlin-type gold deposits: Nature Geoscience, v. 4, p. 122–127.

Palenik, C.S., Utsunomiya, S., Reich, M., Kesler, S.E., Wang, L.M., and Ewing, R.C., 2004, "Invisible" gold revealed: Direct imaging of gold nanoparticles in a Carlin-type deposit: American Mineralogist, v. 89, p. 1359–1366.

Panigrahi, S.K., and Jayaganthan, R., 2010, Effect of annealing on precipitation, microstructural stability, and mechanical properties of cryorolled Al 6063 alloy: Journal of Materials Science, v. 45, p. 5624–5636.

Pettifor, D., 1996, Electron theory of metals, *in* Cahn, R.W., and Haasen, P.,eds., Physical metallurgy[4th ed.]: Amsterdam, Elsevier, p. 47–133.

Putnis, A., 1992, An introduction to mineral sciences: New York, Cambridge University Press, 497 p.

Reich, M., Kesler, S.E., Utsunomiya, S., Palenik, C.S., Chryssoulis, S.L., and Ewing, R.C., 2005, Solubility of gold in arsenian pyrite: Geochimica et Cosmochimica Acta, v. 69, p. 2781–2796.

Reich, M., Utsunomiya, S., Kesler, S.E., Wang, L., Ewing, R.C., and Becker, U., 2006, Thermal behavior of metal nanoparticles in geologic materials: Geology, v. 34, p. 1033–1036.

Ressel, M.W., and Henry, C.D., 2006, Igneous geology of the Carlin trend, Nevada: Development of the Eocene plutonic complex and significance for Carlin-type gold deposits: Economic Geology, v. 101, p. 347–383.

Savage, K.S., Tingle, T.N., O'Day, P.A., Waychunas, G.A., and Bird, D.K.,2000, Arsenic speciation in pyrite and secondary weathering phases, Mother Lode gold district, Tuolumne County, California: Applied Geochemistry, v. 15, p. 1219–1244.

Seward, T.M., 1973, Thio complexes of gold and the transport of gold in hydrothermal ore solutions: Geochimica et Cosmochimica Acta, v. 37, p. 379–399.

Shackelford, J.F., 2016, Introduction to materials science for engineers: Upper Saddle River, Pearson, 687 p.

Simmons, S.F., 2005, Geological characteristics of epithermal precious and base metal deposits: Economic Geology 100th Anniversary Volume, p. 485–522.

Simon, G., Huang, H., Penner-Hahn, J.E., Kesler, S.E., and Kao, L.S., 1999a, Oxidation state of gold and arsenic in gold-bearing arsenian pyrite: American Mineralogist, v. 84, p. 1071–1079.

Simon, G., Kesler, S.E., and Chryssoulis, S., 1999b, Geochemistry and textures of gold-bearing arsenian pyrite, Twin Creeks, Nevada: Implications for deposition of gold in Carlin-type deposits: Economic Geology, v. 94, p. 405–421.

Smith, C.S., 1964, Some elementary principles of polycrystalline microstructure: Metallurgical Reviews, v. 9, p. 1–48.

Stefánsson, A., and Seward, T., 2004, Gold (I) complexing in aqueous sulphide solutions to 500 C at 500 bar: Geochimica et Cosmochimica Acta, v. 68, p. 4121–4143.

Su, W., Xia, B., Zhang, H., Zhang, X., and Hu, R., 2008, Visible gold in arsenian pyrite at the Shuiyindong Carlin-type gold deposit, Guizhou, China: Implications for the environment and processes of ore formation: Ore Geology Reviews, v. 33, p. 667–679.

Su, W., Heinrich, C.A., Pettke, T., Zhang, X., Hu, R., and Xia, B., 2009, Sediment-hosted gold deposits in Guizhou, China: Products of wall-rock sulfidation by deep crustal fluids: Economic Geology, v. 104, p. 73–93.

Su, W., Zhang, H.T., Hu, R.Z., Ge, X., Xia, B., Chen, Y.Y., and Zhu, C., 2012, Mineralogy and geochemistry of gold-bearing arsenian pyrite from the Shuiyindong Carlin-type gold deposit, Guizhou, China: Implications for gold depositional processes: Mineralium Deposita, v. 47, p. 653–662.

Su, W., Dong, W., Zhang, X., Shen, N., Hu, R., Hofstra, A.H., Cheng, L., Xia, Y., and Yang, K., 2018, Carlin-type gold deposits in the Dian-Qian-Gui "Golden Triangle" of southwest China: Reviews in Economic Geology, v. 20, p. 157–185.

Tomkins, A.G., Pattison, D.R.M., and Zaleski, E., 2004, The Hemlo gold deposit, Ontario: An example of melting and mobilization of a precious metal-sulfosalt assemblage during amphibolite facies metamorphism and deformation: Economic Geology, v. 99, p. 1063–1084.

Tomkins, A.G., Pattison, D.R., and Frost, B.R., 2007, On the initiation of metamorphic sulfide anatexis: Journal of Petrology, v. 48, p. 511–535.

Vukmanovic, Z., Reddy, S.M., Godel, B., Barnes, S.J., Fiorentini, M.L., Barnes, S.J., and Kilburn, M.R., 2014, Relationship between microstructures and grain-scale trace element distribution in komatiite-hosted magmatic sulphide ores: Lithos, v. 184–187, p. 42–61.

Widler, A.M., and Seward, T.M., 2002, The adsorption of gold (I) hydrosulphide complexes by iron sulphide surfaces: Geochimica et Cosmochimica Acta, v. 66, p. 383–402.

Williams-Jones, A.E., Bowell, R.J., and Migdisov, A.A., 2009, Gold in solution: Elements, v. 5, p. 281–287.

Wirth, R., 2004, Focused ion beam (FIB): A novel technology for advanced application of micro- and nanoanalysis in geosciences and applied mineralogy: European Journal of Mineralogy, v. 16, p. 863–876.

Wirth, R., Kaminsky, F., Matsyuk, S., and Schreiber, A., 2009, Unusual micro- and nano-inclusions in diamonds from the Juina Area, Brazil: Earth and Planetary Science Letters, v. 286, p. 292–303.

Wirth, R., Reid, D., and Schreiber, A., 2013, Nanometer-sized platinum-group minerals (PGM) in base metal sulfides: New evidence for an orthomagmatic origin of the Merensky reef PGE ore deposit, Bushveld Complex, South Africa: The Canadian Mineralogist, v. 51, p. 143–155.

Xie, Z., Xia, Y., Cline, J.S., Koenig, A., Wei, D., Tan, Q., and Wang, Z., 2018a, Are there Carlin-type gold deposits in China? A comparison of the Guizhou, China, deposits with Nevada, USA, deposits: Reviews in Economic Geology, v. 20, p. 187–233.

Xie, Z., Xia, Y., Cline, J.S., Pribil, M.J., Koenig, A., Tan, Q., Wei, D., Wang, Z., and Yan, J., 2018b, Magmatic origin for sediment-hosted Au deposits, Guizhou Province, China: In situ chemistry and sulfur isotope composition of pyrites, Shuiyindong and Jinfeng deposits: Economic Geology, v. 113, p. 1627–1652.

Xing, Y., Brugger, J., Tomkins, A., and Shvarov, Y., 2019, Arsenic evolution as a tool for understanding formation of pyritic gold ores: Geology, v. 47, p. 335–338.

Xu, H., 2000, Investigation of Invisible Au in Au-bearing FeS_2 microcrystals from Carlin gold ore deposit, Nevada , USA: TEM study and geochemical modeling: Geological Journal of China Universities, v. 6, p. 534–531.

Yoon, M.-S., Park, Y.-J., and Joo, Y.-C., 2002, Impurity redistributions in electroplated Cu films during self-annealing: Thin Solid Films, v. 408, p. 230–235.

Qing-Lin Liang is currently a fifth-year Ph.D. student at the Institute of Geochemistry at the Chinese Academy of Sciences. He received a B.A. degree in geology from the Chengdu University of Technology in 2015. He worked with Richard Wirth as a joint-training Ph.D. student at the German Research Centre for Geosciences, Potsdam, from January to June 2019. His research interest focuses on nanogeosciences, and he mainly works on the distribution of precious metals in sulfides from magmatic sulfide deposits and Carlin-type Au deposits.

Zhuojun Xie graduated from Chang'an University in 2011 with a B.A. degree in mineral resource exploration engineering. He received a Ph.D. in economic geology from the University of the Chinese Academy of Sciences in 2016. From September 2014 to January 2016, he worked with Prof. Jean Cline as a joint-training Ph.D. student at the University of Nevada, Las Vegas. Currently, he is an associate research professor at the Institute of Geochemistry, Chinese Academy of Sciences. His recent research focuses on Carlin-type Au deposits in Guizhou Province, China, and Nevada, USA.